LASER & PHOTONICS REVIEWS
www.lpr-journal.org

Gauge-Flux-Induced Anti-Pt Phase Transitions for Extreme Control of Channel-Drop Tunneling

Chengzhi Qin, Bing Wang, Shanhui Fan,* and Peixiang Lu**

Parity-time (PT) and anti-parity-time (anti-PT) symmetries have provided important guiding principles in the research of non-Hermitian physics. However, realizations of anti-PT symmetry in photonic systems usually rely on optical nonlinearities and indirect-coupling approaches. Here, they apply the channel interference principle mediated by synthetic gauge-flux biasing in open-cavity systems to construct anti-PT symmetries. It is shown that a specific π-flux biasing into a looped-resonator array can force a frequency degeneracy between pairwise Bloch modes therein. By further coupling the array into two external waveguides with tailored positions of ports, the system near the degeneracy point can be described by an anti-PT-symmetric Hamiltonian. When a real gauge-flux detuning is introduced, the system undergoes a spontaneous transition between anti-PT and anti-PT-broken phases, through which the two extreme cases of complete channel-drop tunneling and complete tunneling suppression can be switched. Finally, by superimposing a PT-symmetric term onto the anti-PT-symmetric Hamiltonian via applying an imaginary gauge-flux biasing, extreme channel-drop amplifying effects can be further realized by exciting the "lasing" mode under the critical-coupling condition. The work bridges the physical connection between synthetic gauge field and anti-PT symmetry. This paradigm may also find many applications from optical routing, and switching to buffering and amplifying on a chip–scale platform.

1. Introduction

Channel-drop tunneling, a resonant tunneling process between two continuums of propagating states through localized resonant states, is an important light transfer effect in waveguide-cavity systems.[1–4] The ability to control the tunneling probability, especially to achieve the extreme case of complete tunneling, has been widely applied in wavelength-division-multiplexing optical communications.[1–4] On the other hand, reaching the opposite extreme of complete tunneling suppression has also led to many applications in optical buffering and slow light propagations.[5,6] The physical mechanism underlying channel-drop tunneling is the channel-interference principle, where two or more resonant modes decaying into the same radiation channel experience constructive or destructive interference, leading to the boosting or suppression of total tunneling probability from one port to another. Apart from controlling channel-drop tunneling, channel interference has manifested as a universal design principle for governing light scattering and radiation in various open-cavity systems. Several notable examples include the formations of super/subradiant modes with enhanced/reduced decay rates from channel interference in open rectangular, cylindrical, and double-slit cavities,[7–9] and their extreme cases of bound states in the continuum (BICs), formed by the precise destructive interference of all outgoing radiation channels.[10–12] Accordingly, channel interference has also become a powerful guiding principle in developing highly directional optoelectronic devices and systems.[13,14]

In a seemingly unrelated context, the concepts of parity-time (PT) and anti-parity-time (anti-PT) symmetries, as early established in quantum mechanics, have spawned many light control strategies in non-Hermitian photonics research.[15–22] Compared to the more familiar PT symmetry from the interplay between balanced on-site gain and loss, a less familiar concept is anti-PT symmetry realized through dissipative coupling between two detuned resonances.[19,20] Physically, owing to their similar non-Hermitian origins, the dissipative coupling is closely related to the channel-interference principle, both described by a linear, imaginary coupling rate between two resonances via their energy exchange with the common environment. Since anti-PT results from the dissipative coupling, there should be a physical connection between anti-PT symmetry and the channel-interference effects. This connection, however, has not been previously explored. Moreover, an essential feature of anti-PT-symmetric

C. Qin, B. Wang, P. Lu
Wuhan National Laboratory for Optoelectronics and School of Physics
Huazhong University of Science and Technology
Wuhan, Hubei 430074, China
E-mail: wangbing@hust.edu.cn; lupeixiang@hust.edu.cn
S. Fan
Ginzton Laboratory and Department of Electrical Engineering
Stanford University
Stanford, CA 94305, USA
E-mail: shanhui@stanford.edu
P. Lu
Hubei Key Laboratory of Optical Information and Pattern Recognition
Wuhan Institute of Technology
Wuhan, Hubei 430205, China

The ORCID identification number(s) for the author(s) of this article can be found under https://doi.org/10.1002/lpor.202300458

DOI: 10.1002/lpor.202300458

systems is the phase transition between anti-PT and anti-PT-broken regimes. A further natural question arises as to whether anti-PT phase transition can be harnessed to control channel-drop tunneling probability. This question confronts many challenges due to the difficulties in creating anti-PT symmetries in photonics. Although being early demonstrated in atomic, electrical, and diffusive systems,[23–26] anti-PT symmetries have only recently been achieved in photonic systems through stimulated Brillouin scattering[27,28] or using linear but indirect-coupling approaches,[29–32] which require complex nonlinear processes or specific designed auxiliary elements. In particular, the indirect-coupling approaches only work well for the case of two **spatially-separated** coupled resonators or waveguides,[29–32] which are not applicable to the coupling of two **spatially-overlapped** resonances as usually encountered in the channel-drop tunneling scenarios. To overcome the limitations of optical nonlinearities and indirect-coupling mechanisms, recent attempts have also proposed to apply mechanical spinning for a resonator to realize anti-PT symmetry.[33] In this case, the frequency detuning between two counterpropagating modes is imparted by the spinning-induced Sagnac–Fizeau frequency shift and the dissipative coupling between them is achieved by the backscattering of the tapered waveguide. Although without relying on nonlinearities, the precise spinning of an optical resonator is still technologically challenging.

To overcome all these drawbacks, we propose a linear and direct-coupling scheme using the channel-interference principle mediated by synthetic gauge-flux biasing in open-cavity systems to realize anti-PT symmetries, which inherently applies to the control of channel-drop tunneling. We consider a coupled-resonator array where all the modes are spatially overlapped rather than separated from one another, enabling direct coupling among them. Then a requirement for creating anti-PT symmetry is to force a frequency degeneracy for two appropriate modes. We show that the introduction of a gauge flux biasing into the array can enable the frequency tuning for anti-PT construction. Synthetic gauge field for photons, as the direct analog of real magnetic field for electrons, has emerged as a prerequisite ingredient for emulating photonic topological effects and also a powerful tool for steering light propagation.[34–43] The physical effect of the gauge field is to induce a momentum (phase) shift for the photon through Peierls substitution.[34–43] When applied in a discretized lattice system, the influence of gauge field on the eigen modes is closely related to the lattice's geometry (topology), i.e., the specific boundary conditions. In particular, for a one-dimensional lattice under periodic boundary conditions (PBCs), the gauge field can induce a shift of Bloch momentum, which can be mapped into a shift of eigen frequency through the lattice's band structure.[41–43] Without relying on optical nonlinearities and indirect-coupling methods, the application of synthetic gauge field combined with judicious lattice-geometry design may provide a unique approach to studying anti-PT physics in direct-coupling systems.

Toward this aim, we design looped geometry, coupled microring resonators with PBCs threaded by a synthetic gauge flux introduced using auxiliary rings. The resonator loop is then coupled to two external bus waveguides and is hence naturally dissipative. We reveal that a π-flux biasing in the loop can force a frequency degeneracy between pairwise Bloch modes, near which the system can be described by an anti-PT-symmetric Hamiltonian. By introducing a real gauge-flux detuning from π, we can realize a spontaneous transition between anti-PT and anti-PT-broken phases and achieve the two extreme cases of channel-drop tunneling, switching from complete tunneling to complete tunneling suppression. Moreover, by introducing an imaginary gauge-flux detuning, a PT-symmetric term can also be superimposed into the anti-PT-symmetric Hamiltonian, through which we further realize the extreme channel-drop amplifying by exciting the "**lasing**" mode under critical-coupling condition. Our work reveals a linear, direct-coupling scheme to create anti-PT symmetries, which may also find wide applications in optical routing, switching, buffering, and amplifying for optical communications and signal processing.

2. Construction of Anti-PT Symmetry in Gauge-Flux-Biased Looped Resonator Array

Consider a channel-drop system consisting of a resonator loop threaded by a synthetic gauge flux and side-coupled to two external waveguides, as shown in **Figure 1a**. The resonator loop can be constructed using an array of coupled microring resonators with an even number of $N = 2N_1$ ($N \geq 4$) main rings. The gauge flux stems from the asymmetric coupling coefficients $C_{ccw} = C_0 e^{i\phi} e^{-\kappa}$, $C_{cw} = C_0 e^{-i\phi} e^{\kappa}$ along the counterclockwise (CCW) and clockwise (CW) directions, achieved by incorporating auxiliary ring between adjacent main rings with opposite propagation phases and gain/loss distributions in the interior and exterior half parts. The simplest case with $N = 4$ main rings is shown in Figure 1b and discussed in detail in Section S1 (Supporting Information). Here C_0 is the coupling strength for the case of symmetric coupling and ϕ, κ are real and imaginary coupling phases. The direction-dependent, asymmetric coupling phases impart an effective, complex-valued gauge potential $\tilde{A}_{eff}$ along the array, as defined by the path integral $\phi + i\kappa = \int_n^{n+1} \tilde{A}_{eff}\, dn = \tilde{A}_{eff}$, corresponding to a total gauge flux of $\tilde{\Phi} = \oint \tilde{A}_{eff}\, dn = N(\phi + i\kappa)$ penetrating the whole loop.[38–43] By applying Born–von Karman periodic boundary conditions (PBCs),[41–43] the system can be described by the following tight-binding Hamiltonian

$$H_{PBCs} = \sum_{n=1}^{N} \left(\omega_0 \hat{a}_n^{\dagger} \hat{a}_n + C_0 e^{i\phi} e^{-\kappa} \hat{a}_{n+1}^{\dagger} \hat{a}_n + C_0 e^{-i\phi} e^{\kappa} \hat{a}_n^{\dagger} \hat{a}_{n+1} \right) \quad (1)$$

where $\hat{a}_n^{\dagger}(\hat{a}_n)$ is the creation (annihilation) operator for the whispering-gallery-mode (WGM) in the n-th main ring, ω_0 is the resonant frequency without coupling, and $\hat{a}_n = \hat{a}_{n+N}$ denotes the PBCs.

First, we consider the case with zero imaginary gauge flux $\kappa = 0$, where the gain/loss distribution is absent in the auxiliary ring. Due to the preserved translational symmetry along the lattice direction under PBCs, Equation (1) can support a set of eigen Bloch modes, each of which is described by a real eigen-frequency and a travelling-wave-form eigenstate (see Section S2 for detailed derivation, Supporting Information)

$$\begin{cases} \omega_l = \omega_0 + 2C_0 cos\left(k_l - \Phi/N\right) \\ |\psi_l\rangle = \frac{1}{\sqrt{N}} \left[1, e^{ik_l}, e^{i2k_l}, \ldots, e^{i(N-1)k_l}\right]^T \end{cases} \quad (2)$$

where $\langle \psi_l | \psi_{l'} \rangle = \delta_{ll'}$ satisfies the orthogonal and normalization condition, $k_l = 2\pi l/N$, ($l = 1, 2, \ldots, N$) is the quantized Bloch

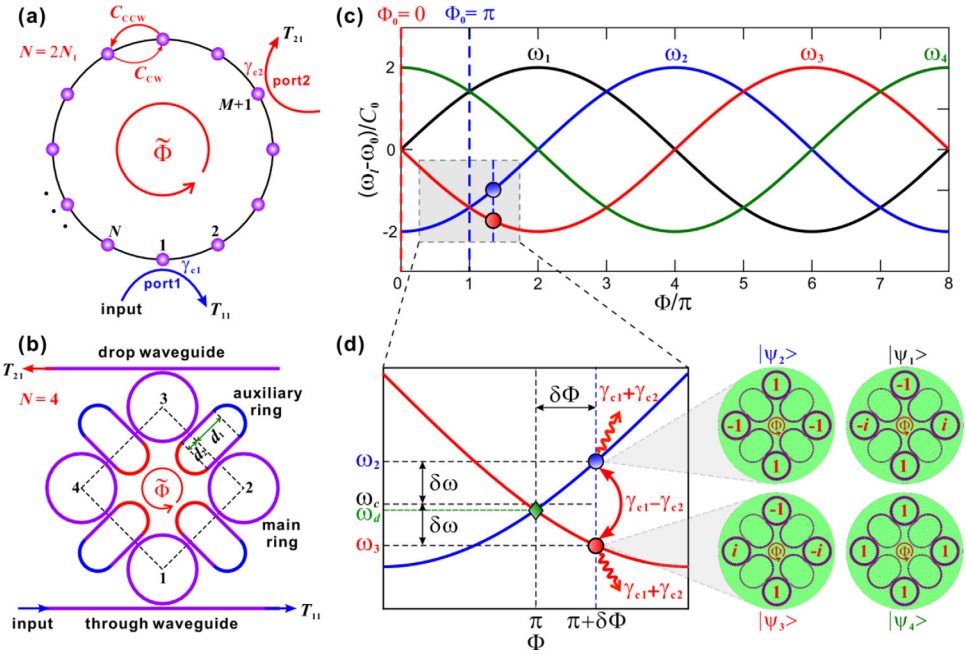

Figure 1. Schematic diagrams of channel-drop tunneling systems and the gauge-flux-induced frequency detuning. a) Schematic of a general channel-drop tunneling system consisting of a close-looped microring resonator array with an even number of $N = 2N_1$ main rings threaded by a complex gauge flux $\tilde{\Phi} = N(\phi + i\kappa)$ and side-coupled to two bus waveguides at ports 1 and 2 spaced by M sites with decay rates γ_{c1} and γ_{c2}. b) The exemplified channel-drop system with $N = 4$ main rings coupled through $N = 4$ auxiliary rings, where the real and imaginary gauge fluxes are provided by the opposite lengths and gain/loss distributions in the auxiliary rings, and d_1, d_2 are length parameters. c) Variation of the eigen-frequencies ω_1, ω_2, ω_3, ω_4 of four Bloch modes versus the real gauge flux Φ. d) Schematic of the gauge-flux-induced frequency detuning between the Bloch-mode pair $|\psi_2\rangle$ and $|\psi_3\rangle$ and their hybridization process near the degeneracy point. The frequencies of two modes are $\omega_2 = \omega_c + \delta\omega$, $\omega_3 = \omega_c - \delta\omega$ under $\Phi = \pi + \delta\Phi$, where ω_c is the central frequency, ω_d is the degenerate frequency under $\Phi = \pi$, $\delta\Phi$ and $\delta\omega$ are gauge-flux detuning from π and the frequency detuning, $\gamma_{c1} + \gamma_{c2}$ is the self-decay rate of each mode and $\gamma_{c1} - \gamma_{c2}$ is the cross-decay rate between them. The right panel shows the simulated mode profiles of the four eigen Bloch modes: $|\psi_2\rangle$, $|\psi_3\rangle$ and $|\psi_1\rangle$ and $|\psi_4\rangle$.

momentum equally distributed in the Brillouin zone due to the PBCs constraint.[41–43] The eigen frequencies of four Bloch modes for $N = 4$ cases are shown in Figure 1c. The introduction of the gauge flux Φ can induce a Bloch momentum shift through Peierls substitution $k_l \to k_l - \Phi/N$, which further induces an eigen-frequency shift to each Bloch mode. Meanwhile, the presence of gauge flux under PBCs does not change the traveling-wave form of the Bloch-mode eigenstate. It should be mentioned that in our system the choice of PBCs is necessary to construct anti-PT symmetry. As we will show below, to realize anti-PT symmetry one should start from a frequency degeneracy point for two chosen modes. With PBC this can be readily achieved by choosing the appropriate gauge flux biasing in the array. By contrast, if we adopt open boundary conditions (OBCs) instead of PBCs, the resonator array supports a set of standing-wave modes instead of traveling-wave Bloch modes for PBCs. The eigenfrequency of each standing-wave mode is $\omega_s = \omega_0 + 2C_0\cos(k_s)$, where $k_s = s\pi/(N+1)$, $s = 1, 2, \ldots, N$ is the mode index, see Section S2 (Supporting Information) for detailed derivation.[41–43] Since the presence of gauge flux Φ under OBCs does not change the eigenfrequency, we can get $\omega_s \neq \omega_{s'}$ for $s \neq s'$ under any choice of Φ, indicating that the introduction of gauge flux under OBCs cannot achieve frequency degeneracy to get anti-PT. Therefore, in our work, the combination of appropriate gauge flux biasing with judicious choices of boundary conditions is essential for the construction of anti-PT symmetries.

To construct an anti-PT-symmetric Hamiltonian, the first requirement is to start from a frequency degeneracy point for two chosen modes. For the case of $N = 4$ shown in Figure 1c and $N = 6, 8$ shown in Figure S2 (Supporting Information), the degeneracy can only occur under an integer multiple of π flux, $\Phi_0 = \pi$, 2π, 3π, etc. Specifically, for an even number of π flux, $\Phi_0 = 2p\pi$ ($p \in \mathrm{Z}$), such as $\Phi_0 = 0$, the modes $|\psi_l\rangle$ and $|\psi_{N-l}\rangle$ are degenerate at $\omega_l = \omega_{N-l} = \omega_d = \omega_0 + 2C_0\cos(k_l)$, ($l = 1,\ldots, N/2-1$), while the left two modes $|\psi_{N/2}\rangle$ and $|\psi_N\rangle$ cannot find degenerate partners. For $N = 4$ as an example, we get only one degenerate mode pair $\omega_1 = \omega_3 = \omega_0 + 2C_0\cos(k_1) = \omega_0$ and two non-degenerate ones $\omega_2 = \omega_0 + 2C_0\cos(k_2) = \omega_0 - 2C_0$, $\omega_4 = \omega_0 + 2C_0\cos(k_4) = \omega_0 + 2C_0$. While for an odd number of π flux, $\Phi_0 = (2p+1)\pi$ ($p \in \mathrm{Z}$), all the $N = 2N_1$ modes can be divided into N_1 degenerate mode pairs. In particular, for $\Phi_0 = \pi$, the modes $|\psi_l\rangle$ and $|\psi_{N+1-l}\rangle$ are degenerate at $\omega_l = \omega_{N+1-l} = \omega_d = \omega_0 + 2C_0\cos(k_l - \pi/N)$, ($l = 1,\ldots, N/2-1$). For the two cases, the degenerate mode pair can be uniformly denoted by $|\psi_l\rangle$ and $|\psi_{l'}\rangle$, where $l' = N - l$ or $l' = N + 1 - l$ for $\Phi_0 = 0$ or π, respectively. In the vicinity of the degeneracy point, as Φ is slightly detuned from Φ_0 by $\delta\Phi$, i.e., $\Phi = \Phi_0 + \delta\Phi$, there will emerge a frequency detuning between the mode pair

$$\begin{cases} \omega_l = \omega_0 + 2C_0\cos(k_l - \Phi_0/N - \delta\Phi/N) = \omega_c + \delta\omega \\ \omega_{l'} = \omega_0 + 2C_0\cos(k_{l'} - \Phi_0/N - \delta\Phi/N) = \omega_c - \delta\omega \end{cases} \quad (3)$$

where $\omega_c = \omega_0 + 2C_0\cos(k_l - \Phi_0/N)\cos(\delta\Phi/N) \approx \omega_d$, $\delta\omega = 2C_0\sin(k_l - \Phi_0/N)\sin(\delta\Phi/N)$ are central frequency and frequency

detuning between the two modes. The gauge-flux detuning induced frequency detuning for the $N = 4$ case is shown in Figure 1d, where there are two degenerate mode pairs $\omega_1 = \omega_4 = \omega_0 + \sqrt{2}C_0$, $\omega_2 = \omega_3 = \omega_0 - \sqrt{2}C_0$ under $\Phi_0 = \pi$, near which $\delta\omega$ can be continuously tuned by the gauge-flux detuning $\delta\Phi$.

After obtaining the frequency detuning, the second requirement is to create a dissipative (imaginary) coupling between these two modes for anti-PT construction. Here the dissipative coupling stems from the radiation interference between these two modes into the two external waveguides via two ports 1 and 2. As shown in Figure 1a, we start from the most general case where the two waveguides are connected at $n = 1$ and $n = M + 1$ main rings, giving rise to a site interval of M between the two ports. Here M can take the value of 1, 2,..., N−2, and the specific case of $M = N/2 = N_1$ is illustrated in Figure 1b. For light incidence from port 1 at the frequency near ω_c, it will simultaneously excite these two modes which will in turn decay back into the two waveguides. In terms of temporal-coupled-mode theory (TCMT),[44–47] the interference of radiation between the two modes can be described by a 2 × 2 out-coupling matrix

$$D = \begin{pmatrix} D_{1,l} & D_{1,l'} \\ D_{2,l} & D_{2,l'} \end{pmatrix} = \begin{pmatrix} \sqrt{2\gamma_{c1}} & \sqrt{2\gamma_{c1}} \\ \sqrt{2\gamma_{c2}}e^{iMk_l} & \sqrt{2\gamma_{c2}}e^{iMk_{l'}} \end{pmatrix} \tag{4}$$

where $D_{n,l}$ denotes the coupling coefficient from mode $|\psi_l\rangle$ to port $n = 1, 2$, which is proportional to the respective modal profile at $n = 1$ and $n = M + 1$ main rings. γ_{c1}, γ_{c2} are the decay rates of the two modes at the two ports. According to the energy-conservation condition,[44–47] we can obtain the joint decay matrix for the two modes

$$\Gamma_c = \frac{D^\dagger D}{2} = \begin{pmatrix} \gamma_{c1} + \gamma_{c2} & \gamma_{c1} + \gamma_{c2}e^{i\theta} \\ \gamma_{c1} + \gamma_{c2}e^{-i\theta} & \gamma_{c1} + \gamma_{c2} \end{pmatrix} \tag{5}$$

where

$$\theta = M(k_{l'} - k_l) \tag{6}$$

which denotes the **propagation phase difference** of the two modes between the two ports. As shown in Figure 1d, the diagonal element of Γ_c is the total self-decay rate of each mode into the two ports, while the off-diagonal element is the cross-decay rate of the two modes, which accounts for the channel interference between them. By applying quasi-normal-mode (QNM) theory regarding all channels as outgoing radiation boundary conditions,[47,48] we can obtain an effective non-Hermitian Hamiltonian $H_{\text{eff}} = \Omega - i\Gamma_c$ to describe the radiation interference between the two modes, where $\Omega = [\omega_l, 0; 0, \omega_{l'}]$ is the eigen-frequency matrix. By combining with Equations (3) and (5), we can write down H_{eff}

$$H_{\text{eff}} = \begin{pmatrix} \omega_c + \delta\omega & 0 \\ 0 & \omega_c - \delta\omega \end{pmatrix} - i\begin{pmatrix} \gamma_{c1} + \gamma_{c2} & \gamma_{c1} + \gamma_{c2}e^{i\theta} \\ \gamma_{c1} + \gamma_{c2}e^{-i\theta} & \gamma_{c1} + \gamma_{c2} \end{pmatrix} \tag{7}$$

For H_{eff} to be a standard anti-PT-symmetric Hamiltonian, the cross-decay rate should be purely imaginary, which further requires $\theta = 0$ or $\theta = \pi$. Specifically, for the case of $\Phi_0 = 0$, we can get $\theta = M(k_{l'} - k_l) = M[2\pi(N-l)/N - 2\pi l/N] = -2\pi lM/N_1$. To reach $\theta = 0$ for each l, we should choose $M = N_1$, where the two ports are located at the opposite sites in the resonator loop, as typically shown in Figure 1b for the $N = 4$ case. For $\Phi_0 = \pi$, we have $\theta = M(k_{l'} - k_l) = M[2\pi(N + 1 - l)/N - 2\pi l/N] = \pi(1-2l)M/N_1$. In this case, we can also choose $M = N_1$ to get $\theta = \pi$. Note that for $\Phi_0 = 0$, the modes $|\psi_{N/2}\rangle$ and $|\psi_N\rangle$ cannot find degenerate mode partners to form anti-PT symmetry. Moreover, $\theta = 0$ means the full constructive interference between the two modes, which cannot be harnessed to realize the complete tunneling suppression as is shown below. Thus throughout the paper, we only choose $\Phi_0 = \pi$ and $M = N_1$ to construct anti-PT symmetry that is applicable to all Bloch modes. The analysis of a general case with an arbitrary port configuration is shown in Section S5 (Supporting Information). For $\Phi_0 = \pi$ and $M = N_1$, the effective Hamiltonian can be rewritten as

$$H_{\text{eff}} = \begin{pmatrix} \omega_c + \delta\omega & 0 \\ 0 & \omega_c - \delta\omega \end{pmatrix} - i\begin{pmatrix} \gamma_{c1} + \gamma_{c2} & \gamma_{c1} - \gamma_{c2} \\ \gamma_{c1} - \gamma_{c2} & \gamma_{c1} + \gamma_{c2} \end{pmatrix} \tag{8}$$

By diagonalizing H_{eff}, we can obtain the eigen-frequencies for the two hybridized modes

$$\tilde{\omega}_\pm = \omega_c - i(\gamma_{c1} + \gamma_{c2}) \pm \sqrt{(\delta\omega)^2 - (\gamma_{c1} - \gamma_{c2})^2} \tag{9}$$

The full phase diagram for an anti-PT phase transition is shown in **Figure 2a**, where the system exhibits an exceptional point (EP) when the frequency detuning reaches $|\delta\omega| = |\delta\omega_{\text{EP}}| = |\gamma_{c1} - \gamma_{c2}|$. As $\delta\omega$ varies across $\delta\omega_{\text{EP}}$, the system undergoes a spontaneous anti-PT phase transition, which is accompanied by the energy-spectrum transition from the decay-rate bifurcation $\tilde{\omega}_\pm = \omega_c - i[(\gamma_{c1} + \gamma_{c2}) \mp \sqrt{(\gamma_{c1} - \gamma_{c2})^2 - (\delta\omega)^2}]$ to the real-frequency bifurcation $\tilde{\omega}_\pm = [\omega_c \pm \sqrt{(\delta\omega)^2 - (\gamma_{c1} - \gamma_{c2})^2}] - i(\gamma_{c1} + \gamma_{c2})$. Since $\delta\omega = 2C_0\sin(k_l - \Phi_0/N)\sin(\delta\Phi/N) \propto \delta\Phi$ for a tiny $\delta\Phi$, the frequency detuning can be tuned by gauge-flux detuning in a linear fashion shown in Figure 2b. Therefore, we can induce anti-PT phase transition by proportionally increasing the gauge flux detuning. As we will demonstrate below, by exploiting anti-PT phase transition, we can further achieve versatile extreme control over the channel-drop tunneling effects.

The rigorous channel-drop tunneling transmittance spectrum can be obtained by applying TCMT,[44–47] which reads

$$\begin{cases} \frac{d}{dt}|\Psi\rangle = -iH_{\text{eff}}|\Psi\rangle + K^T|s_+\rangle \\ |s_-\rangle = C|s_+\rangle + D|\Psi\rangle \end{cases} \tag{10}$$

where $|\Psi\rangle = (a_1, a_2, ..., a_N)^T$ is the normalized mode amplitude involving all N Bloch modes, $|s_+\rangle = (s_{1+}, 0)^T$, $|s_-\rangle = (s_{1-}, s_{2-})^T$ are the input and output amplitudes in the two waveguides, for which we consider only light input from the bottom waveguide. C is the direct reflection coefficient matrix at the two ports, K^T, D are $2 \times N$ matrices denoting the in-coupling and out-coupling coefficients between all Bloch modes and the two waveguide modes. By applying time-reversal symmetry conditions,[44–47] we can obtain $C = -\mathbf{I}_2$, where $\mathbf{I}_2$ is 2×2 identity matrix, and

$$\begin{aligned} K^* = D &= \begin{pmatrix} D_{1,1} & D_{1,2} & \cdots & D_{1,N} \\ D_{2,1} & D_{2,2} & \cdots & D_{2,N} \end{pmatrix} \\ &= \begin{pmatrix} \sqrt{2\gamma_{c1}} & \sqrt{2\gamma_{c1}} & \cdots & \sqrt{2\gamma_{c1}} \\ \sqrt{2\gamma_{c2}}e^{iMk_1} & \sqrt{2\gamma_{c2}}e^{iMk_2} & \cdots & \sqrt{2\gamma_{c2}}e^{iMk_N} \end{pmatrix} \end{aligned} \tag{11}$$

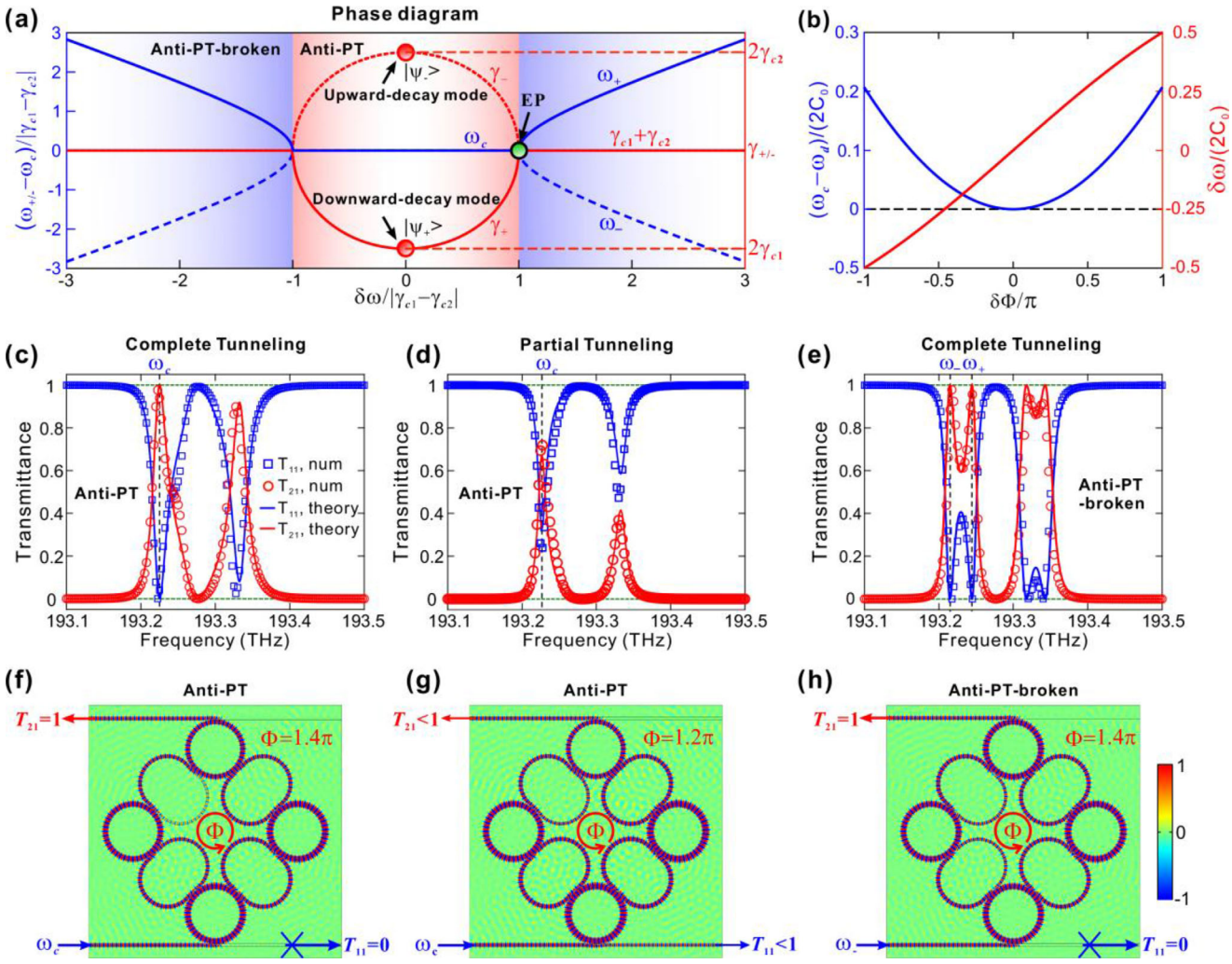

Figure 2. Phase diagram of anti-PT phase transitions and associated channel-drop tunneling effects. a) Phase diagram of anti-PT phase transition: The complex eigen-frequencies of the two hybridized modes versus frequency detuning $\delta\omega$. At $\delta\omega = 0$, the two hybridized modes become downward- and upward-decay modes of $|\psi_{\pm}\rangle$. b) Variations of central frequency ω_c and frequency detuning $\delta\omega$ versus the gauge flux detuning $\delta\Phi$. c,d) Channel-drop tunneling transmittance spectra of T_{11} and T_{21} in the anti-PT regime. The solid and circle curves denote the theoretical and simulated results, respectively. In c and d, the gap between adjacent main and auxiliary rings is $g_0 = 260$ nm, and the gaps at the bottom and top waveguides are $g_1 = 350$ nm and $g_2 = 220$ nm. The gauge fluxes are $\Phi = 1.4\pi$ and $\Phi = 1.2\pi$ in (c) and d. e) Channel-drop tunneling transmittance spectrum in the anti-PT-broken regime. The gaps are $g_0 = 260$ nm and $g_1 = g_2 = 320$ nm. f,g,h) Simulated field distributions for the above three cases in (c, d, e), for light excitation from the bottom waveguide at the peak frequency in the transmittance spectrum.

which is the complete form of Equation (4) by generalizing from the two degenerate modes to all N modes. In Equation (10), $H_{\text{eff}} = \Omega - i\Gamma_c$ is also the complete form of effective Hamiltonian of Equation (7), where Ω is the eigen-frequency matrix with nonzero diagonal element $[\Omega]_{l,l'} = \omega_l$, $\Gamma_c = D^{\dagger}D/2$ is the complete joint decay matrix of Equation (5), with the matrix element given by $[\Gamma_c]_{l,l'} = \gamma_{c1} + \gamma_{c2}\exp[iM(k_{l'} - k_l)]$.

For monochromatic light excitation at frequency ω, the mode amplitude evolves as $d|\Psi\rangle/dt = -i\omega\mathbf{I}_N|\Psi\rangle$, where $\mathbf{I}_N$ is the $N\times N$ identity matrix. By combining with Equation (10), we can get $|s_-\rangle = S(\omega)|s_+\rangle$, where the scattering matrix is $S(\omega) = C + D[-i(\omega\mathbf{I}_N - H_{\text{eff}})]^{-1}K^T$, from which we can obtain the transmittance spectra $T_{11}(\omega) = |S_{11}(\omega)|^2$, $T_{21}(\omega) = |S_{21}(\omega)|^2$ in the through and drop waveguides. Since ω–ω_c, it is safe to only consider the two modes' contributions, which gives rise to the closed-form transmittance spectra (see Section S3 for detailed derivation, Supporting Information)

$$\begin{cases} T_{11}(\omega) = \dfrac{[4\gamma_{c1}\gamma_{c2} + (\omega-\omega_c)^2 - (\delta\omega)^2]^2 + 4(\omega-\omega_c)^2(\gamma_{c2}-\gamma_{c1})^2}{[4\gamma_{c1}\gamma_{c2} - (\omega-\omega_c)^2 + (\delta\omega)^2]^2 + 4(\omega-\omega_c)^2(\gamma_{c2}+\gamma_{c1})^2} \\ T_{21}(\omega) = \dfrac{16\gamma_{c1}\gamma_{c2}(\delta\omega)^2}{[4\gamma_{c1}\gamma_{c2} - (\omega-\omega_c)^2 + (\delta\omega)^2]^2 + 4(\omega-\omega_c)^2(\gamma_{c2}+\gamma_{c1})^2} \end{cases} \tag{12}$$

where $T_{11}(\omega) + T_{21}(\omega) = 1$, indicating the energy-conservation condition in the two waveguides. By changing the frequency detuning through varying gauge-flux detuning, we can continu-

ously tune the transmittance T_{21} from zero fully to unity. In particular, we are interested in the two extreme cases of complete channel-drop tunneling with $T_{21} = 1$, $T_{11} = 0$ and complete tunneling suppression with $T_{21} = 0$, $T_{11} = 1$, where the incident light is completely transferred into the through and drop waveguides, respectively. Below, we will identify the conditions to realize the two extreme cases and reveal the role of anti-PT phase transition in realizing them.

3. Complete Channel-Drop Tunneling with Anti-PT Phase Transitions

First, we consider the extreme case of complete channel-drop tunneling with $T_{11} = 0$, $T_{21} = 1$. According to Equation (12), this case can be achieved by reaching the transmittance *zeros* of T_{11}, which requires

$$\begin{cases} 4\gamma_{c1}\gamma_{c2} + (\omega - \omega_c)^2 - (\delta\omega)^2 = 0 \\ (\omega - \omega_c)^2(\gamma_{c2} - \gamma_{c1})^2 = 0 \end{cases} \tag{13}$$

Case 1: For each mode pair, there is only one frequency where the transmittance *zero* is reached, the frequency can only be $\omega = \omega_c$. The frequency detuning should take the critical value

$$|\delta\omega| = |\delta\omega_{\text{critical}}| = 2\sqrt{\gamma_{c1}\gamma_{c2}} \tag{14}$$

Since the system exhibits anti-PT phase transition at EPs with $|\delta\omega| = |\delta\omega_{\text{EP}}| = |\gamma_{c1} - \gamma_{c2}|$, it is thus necessary to compare these two critical values to determine whether complete tunneling occurs in the anti-PT or anti-PT-broken regime. If complete tunneling occurs in the anti-PT regime, we have $2\sqrt{\gamma_{c1}\gamma_{c2}} < |\gamma_{c1} - \gamma_{c2}|$, which further requires $\gamma_{c2}/\gamma_{c1} > 3 + 2\sqrt{2}$ or $0 < \gamma_{c2}/\gamma_{c1} < 3 - 2\sqrt{2}$. On the contrary, if complete tunneling occurs in the anti-PT-broken regime, the condition should be $3 - 2\sqrt{2} < \gamma_{c2}/\gamma_{c1} < 3 + 2\sqrt{2}$. So, the singe-frequency complete channel-drop tunneling tends to occur in the anti-PT regime for highly asymmetric channel-drop systems and in anti-PT-broken regime for the systems with comparable γ_{c1} and γ_{c2}. Case 2: There are two transmittance *zeros* for each mode pair, the two frequencies are $\omega_{1,2} = \omega_c \pm \sqrt{(\delta\omega)^2 - 4\gamma_{c1}\gamma_{c2}}$ in Equation (12), where $\delta\omega$ should satisfy $|\delta\omega| \geq 2\sqrt{\gamma_{c1}\gamma_{c2}}$ to keep $\omega_{1,2}$ in the real-frequency axis. Meanwhile, the additional constraint on the two decay rates is $\gamma_{c1} = \gamma_{c2}$, indicating the thresholdless feature for the anti-PT phase transition with $|\delta\omega_{\text{EP}}| = |\gamma_{c1} - \gamma_{c2}| = 0$. Accordingly, there will emerge double peaks in the transmittance spectrum for each degenerate mode pair.

The theoretical analysis of complete channel-drop tunneling has also been verified by numerical simulations using COMSOL Multiphysics. In the simulations, we choose the case of $N = 4$ and use Si_3N_4 waveguides with refractive index $n_0 = 2$ and width $W = 0.5$ μm. By operating at telecommunication wavelength $\lambda_0 = 1.55$ μm, we can obtain an effective mode index $n_{\text{eff}} = 1.7512$ and mode wavelength $\lambda_m = \lambda_0/n_{\text{eff}} = 0.8851$ μm. The average radii of the main and auxiliary rings are $R_1 = R_2 = 8.3848$ μm, satisfying $2\pi R_{1,2} = m_{1,2}\lambda_m$, where $m_1 = m_2 = 40$ is the azimuthal longitudinal order of the WGM. Figure 2c shows the transmittance spectrum for the single-frequency complete channel-drop tunneling case, where we fix the gap at $g_0 = 260$ nm between adjacent main and auxiliary rings to get $C_0/2\pi = 38$ GHz. The lengths of the straight-waveguide parts in the auxiliary rings are $d_{1,2} = [2 + 1/8 \pm (1/16 + 1/40)]\lambda_m$, corresponding to a total real gauge flux of $\Phi = 2\pi N(d_1 - d_2)/\lambda_m = \pi + 0.4\pi$, where $\delta\Phi = 0.4\pi$ is the gauge-flux detuning from $\Phi_0 = \pi$. With these length parameters, the anti-resonant condition $2(d_1 + d_2) = (8 + 1/2)\lambda_m$ is satisfied in the auxiliary ring.[38–43] According to Figure 2b, the gauge-flux detuning $\delta\Phi = 0.4\pi$ corresponds to a frequency detuning $|\delta\omega| \approx 0.44C_0$. In addition, the two decay rates are chosen as $\gamma_{c1} = 0.07C_0$, $\gamma_{c2} = 9\gamma_{c1}$ by setting the bottom and top ring-waveguide gaps at $g_1 = 350$ nm and $g_2 = 220$ nm, which satisfies $\gamma_{c2}/\gamma_{c1} = 9 > 3 + 2\sqrt{2}$ and $|\delta\omega_{\text{critical}}| = 2\sqrt{\gamma_{c1}\gamma_{c2}} \sim 0.42C_0$. In this case, we can obtain $|\delta\omega| \approx |\delta\omega_{\text{critical}}|$, where the single-frequency complete channel-drop tunneling condition of Equation (14) is satisfied.

As shown by the simulated transmittance spectra denoted by the circle and square curves in Figure 2c, the complete channel-drop tunneling occurs at $\omega = \omega_c$ for the mode pair $|\psi_2\rangle$ and $|\psi_3\rangle$, which coincides well with the theoretically computed results (solid curves) using Equation (10). Note that the transmittance peak at the degeneracy frequency of $|\psi_1\rangle$, $|\psi_4\rangle$ does not reach unity. This is attributed to the tiny differences in decay rates γ_{c1} and γ_{c2} for $|\psi_1\rangle$, $|\psi_4\rangle$ compared to those of $|\psi_2\rangle$, $|\psi_3\rangle$. For comparison, we also simulate the partial channel-drop tunneling case by reducing the gauge-flux detuning by half to $\delta\Phi = 0.2\pi$ while keeping γ_{c1} and γ_{c2} unchanged. As shown in Figure 2d, the peak transmittance T_{21} does not reach unity, which also matches well with the theoretical curve. Both cases of complete and partial channel-drop tunneling have been verified by the simulated field distributions in Figure 2f,g, where the input light manifests full or partial tunneling in the drop waveguide. On the other hand, to achieve double-frequency complete channel-drop tunneling in the anti-PT-broken regime, we fix the gauge flux at $\Phi = \pi + 0.4\pi$, with $\delta\Phi = 0.4\pi$ and choose a symmetric channel-drop system with $\gamma_{c1} = \gamma_{c2} = 0.1C_0$ by setting $g_1 = g_2 = 320$ nm. The double-peak feature truly emerges in the theoretical and numerical transmittance spectra shown in Figure 2e, which is also well evidenced by the simulated field distribution shown in Figure 2h.

4. Broadband, Complete Channel-Drop Tunneling Suppression in the Anti-PT Regime

On the contrary, we can also achieve the other extreme of complete channel-drop tunneling suppression by reaching the degeneracy point under zero gauge-flux detuning. By setting $\delta\omega = 0$ in Equation (12), we find that $\boldsymbol{T_{11}(\omega) \equiv 1}$, $\boldsymbol{T_{21}(\omega) \equiv 0}$ can be fulfilled for any input frequency (see Section S3 for detailed derivation, Supporting Information), indicating that the complete tunneling suppression is a broadband behavior. **Figure 3a** shows the simulated transmittance spectrum for the $N = 4$ case, which shows the flat transmittance spectrum for the complete tunneling suppression. To explain the underneath mechanism, let us check the hybridized modes at the degeneracy point

$$\tilde{\omega}_{\pm} = \omega_l - i(\gamma_{c1} + \gamma_{c2}) \pm [-i(\gamma_{c1} - \gamma_{c2})] = \begin{cases} \omega_l - i2\gamma_{c1} (\text{downward-decay mode}) \\ \omega_l - i2\gamma_{c2} (\text{upward-decay mode}) \end{cases} \tag{15}$$

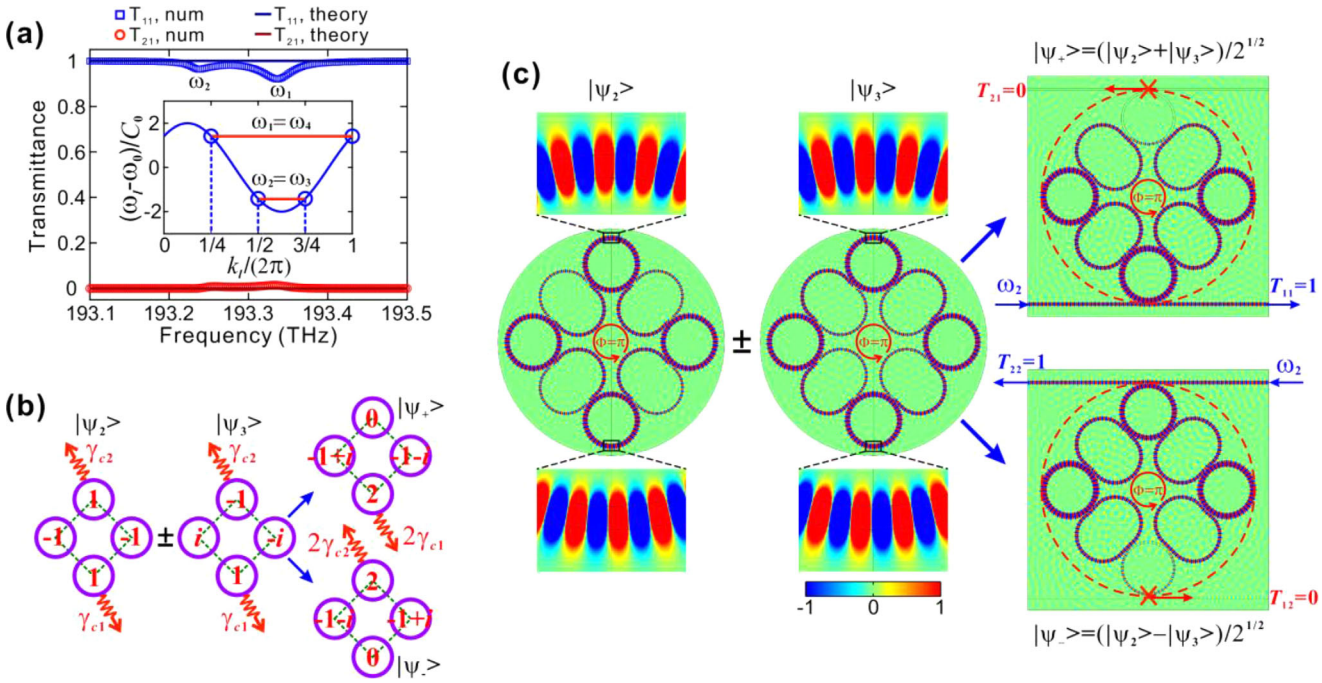

Figure 3. Transmittance spectrum for complete channel-drop tunneling suppression case and a schematic sketch of the forming of unidirectional-decayed modes. a) Channel-drop tunneling transmittance spectra T_{11} and T_{21} at degeneracy point of $\delta\omega = 0$ under $\Phi = \pi$. The solid and circle curves are theoretical and simulated results. The inset figure denotes the eigen-frequencies of the four Bloch modes, showing two degenerate mode pairs of $\omega_1 = \omega_4$ and $\omega_2 = \omega_3$. b) Mode profiles of $|\psi_2\rangle$ and $|\psi_3\rangle$ and their interference to form downward- and upward-decayed modes $|\psi_\pm\rangle$. c) Simulated field distributions of $|\psi_2\rangle$, $|\psi_3\rangle$ and $|\psi_\pm\rangle = (|\psi_2\rangle \pm |\psi_3\rangle)/\sqrt{2}$, obtained by exciting from bottom and top waveguides. The zoom-in figures represent the detailed mode profiles showing the phase distributions of $|\psi_2\rangle$, $|\psi_3\rangle$ at the bottom and top rings.

corresponding to the two hybridized eigenstates

$$|\psi_\pm\rangle = \frac{1}{\sqrt{2}}\left(|\psi_l\rangle \pm |\psi_{N+1-l}\rangle\right) \tag{16}$$

which are formed by the symmetric and antisymmetric superpositions of $|\psi_l\rangle$ and $|\psi_{N+1-l}\rangle$ with an equal weight factor of 1:±1. It is easy to check the orthogonal and normalization condition for the two hybridized modes: $\langle\psi_+|\psi_+\rangle = \langle\psi_-|\psi_-\rangle = 1$, $\langle\psi_+|\psi_-\rangle = \langle\psi_-|\psi_+\rangle = 0$. After hybridization with identical weight factor, the original **bidirectionally-decayed** modes $|\psi_l\rangle$ and $|\psi_{N+1-l}\rangle$ with the same decay rate of $\gamma_{c1} + \gamma_{c2}$ into the two waveguides transform into **unidirectionally-decayed** modes $|\psi_\pm\rangle$ with decay rates $2\gamma_{c1}$ and $2\gamma_{c2}$ into only bottom or top waveguide. This hybridization process of $|\psi_2\rangle$ and $|\psi_3\rangle$ for the $N = 4$ case is shown in Figure 3b. Here $|\psi_\pm\rangle = (|\psi_2\rangle \pm |\psi_3\rangle)/\sqrt{2} = [(1,-1,1,-1)^T/2 \pm (1,-i,-1,i)^T/2]/\sqrt{2} = (2,-1-i,0,-1+i)^T/2\sqrt{2}$ and $(0,-1+i,2,-1-i)^T/2\sqrt{2}$, indicating the vanishing mode amplitude of $|\psi_+\rangle$ ($|\psi_-\rangle$) at the top (bottom) main ring due to the destructive interference of $|\psi_2\rangle$ and $|\psi_3\rangle$ therein, giving rise to the unidirectional decay downward (upward) into the bottom or top waveguide, respectively. The interference feature is also embodied in the out-coupling matrix D for $|\psi_+\rangle$ in Equation (4), where $D_{1,l} = D_{1,l'}$, $D_{2,l} + D_{2,l'} = 0$, showing the constructive and destructive interference of $|\psi_l\rangle$ and $|\psi_{l'}\rangle$ at ports 1 and 2.

As shown by the simulation in Figure 3c, $|\psi_+\rangle$ ($|\psi_-\rangle$) can be excited directly from the bottom (top) waveguide with arbitrary frequency, which will lead to complete tunneling suppression on the other side. The excitation of $|\psi_+\rangle$ or $|\psi_-\rangle$ alone but not both can be verified by calculating the static mode coefficients in the resonator array under light excitation from one bus waveguide. For example, for light input from the bottom waveguide, according to Equation (10), we can obtain the mode coefficients (see Section S3 for derivation, Supporting Information)

$$\begin{aligned}|\Psi\rangle &= \left(a_l, a_{N+1-l}\right)^T = \left[-i(\omega\mathbf{I}_2 - H_{\text{eff}})\right]^{-1} K^T |s_+\rangle \\ &\propto \left[-i(\omega - \omega_c + \delta\omega) + 2\gamma_{c2}, -i(\omega - \omega_c - \delta\omega) + 2\gamma_{c2}\right]^T\end{aligned} \tag{17}$$

from which we have $(a_l, a_{N+1-l})^T \propto (1,1)^T = \psi_+$ for $\delta\omega = 0$, meaning that only ψ_+ is excited. This analysis is also applicable to the excitation from the right end of the top waveguide.

The effect of complete tunneling suppression under π-flux biasing is a universal behavior, which can be generalized to the case with an arbitrary even number of main rings $N = 2N_1$. The two exemplified cases of $N = 6$ and 8 are shown in **Figure 4**, both of which manifest complete tunneling suppression features over a broadband regime both for the bottom and up waveguide excitations. The degenerate mode pairs are indicated by the inserted figures in Figure 4a,d, which read $\omega_1 = \omega_6 = \omega_0 + \sqrt{3}C_0$, $\omega_2 = \omega_5 = \omega_0$, $\omega_3 = \omega_4 = \omega_0 - \sqrt{3}C_0$ for $N = 6$ and $\omega_1 = \omega_8 = \omega_0 + 2C_0\cos(\pi/8)$, $\omega_2 = \omega_7 = \omega_0 + 2C_0\cos(3\pi/8)$, $\omega_3 = \omega_6 = \omega_0 + 2C_0\cos(5\pi/8)$, $\omega_4 = \omega_5 = \omega_0 + 2C_0\cos(7\pi/8)$ for $N = 8$. More detailed discussions about the modal profiles of these degenerate mode pairs are shown in Section S4 (Supporting Information).

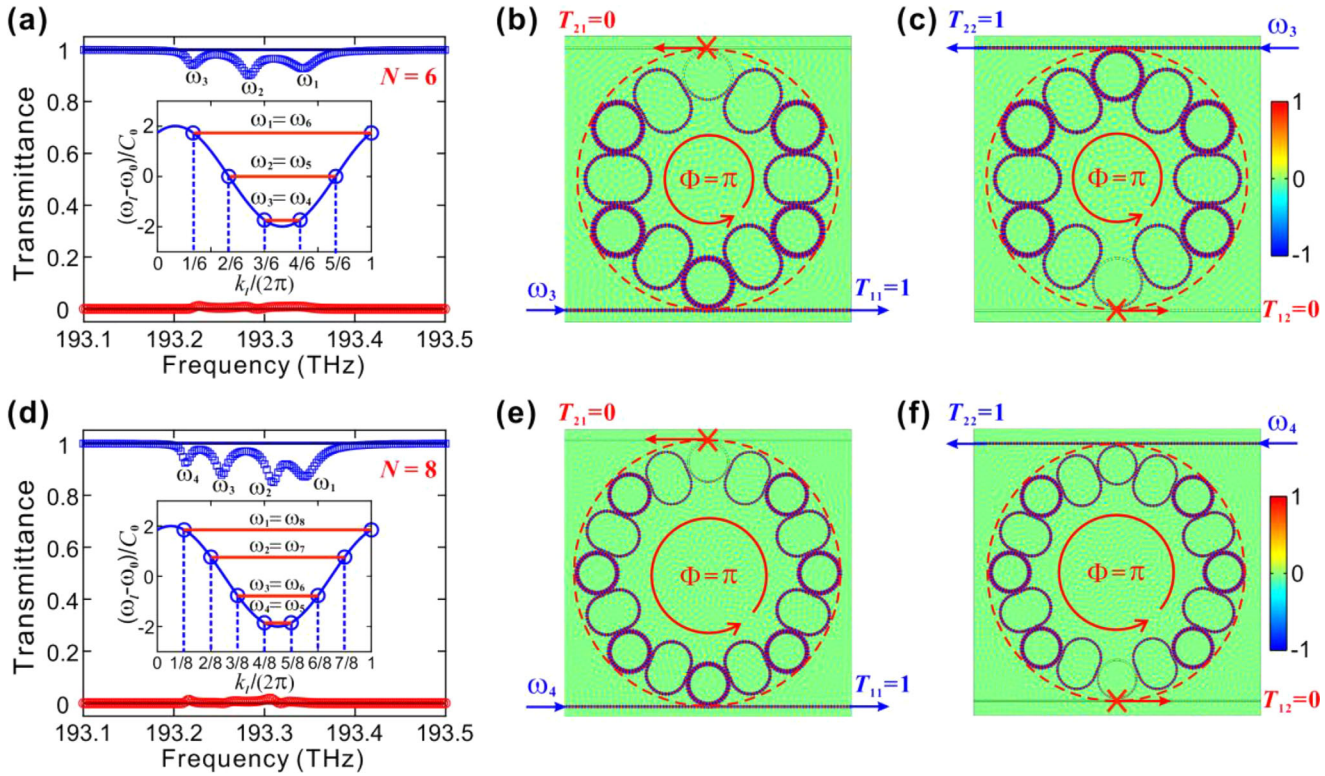

Figure 4. Complete channel-drop tunneling suppression for $N = 6$ and 8 cases. a) Channel-drop tunneling transmittance spectra T_{11} and T_{21} for $N = 6$ under π-flux biasing. The inset figure shows the band structure of the looped resonator array and eigen-frequencies of six Bloch modes, forming three degenerate mode pairs $\omega_1 = \omega_6$, $\omega_2 = \omega_5$, $\omega_3 = \omega_4$. b,c) Simulated field distributions for light input from the bottom and top waveguides at the frequency $\omega = \omega_3$. d,e,f) The similar figures with (a,b,c) but for $N = 8$. In this case, there are four degenerate mode pairs $\omega_1 = \omega_8$, $\omega_2 = \omega_7$, $\omega_3 = \omega_6$, $\omega_4 = \omega_5$.

The demonstrations prove the universality and scalability of the broadband complete tunneling suppression effect under π-flux biasing.

5. Channel-Drop Amplifying Effects under Imaginary Gauge-Flux Biasing

The above analysis is based on a purely passive system without light amplification, in this section we will extend to an active system to achieve channel-drop amplifying effects. To this aim, we apply an additional imaginary gauge flux biasing with $\kappa \neq 0$ superimposed onto the original real gauge flux by introducing the simultaneous gain/loss distributions in the auxiliary rings,[41–43] as shown in Figure 1b. To keep the mode degeneracy unchanged, we fix the real gauge flux at $\Phi_0 = \pi$, such that the total complex-valued gauge flux is $N(\phi + i\kappa) = \pi + iN\kappa$. The eigen frequencies of all Bloch modes also become complex-valued $\omega_l - i\gamma_l$, which read

$$\begin{cases} \omega_l = \omega_0 + 2C_0 \cosh(\kappa) \cos(k_l - \phi) \\ \gamma_l = -2C_0 \sinh(\kappa) \sin(k_l - \phi) \end{cases} \tag{18}$$

from which we can find $\gamma_{N+1-l} = -\gamma_l$, meaning that the additional imaginary gauge-flux biasing can impart an opposite intrinsic gain/loss rate to the degenerate mode pair, as also shown in the insert figure of **Figure** 5a. The balanced gain/loss rates form a PT-symmetric term superimposed onto the original anti-PT-symmetric Hamiltonian, which gives rise to a modified Hamiltonian

$$H_{\text{eff}} = \begin{pmatrix} \omega_c - i\gamma_l & 0 \\ 0 & \omega_c + i\gamma_l \end{pmatrix} - i \begin{pmatrix} \gamma_{c1} + \gamma_{c2} & \gamma_{c1} - \gamma_{c2} \\ \gamma_{c1} - \gamma_{c2} & \gamma_{c1} + \gamma_{c2} \end{pmatrix} \tag{19}$$

By comparing with Equation (8), we find that the imaginary gauge-flux detuning can induce a decay-rate detuning $2i\gamma_l$ for the two modes, which is different from the real gauge-flux induced frequency detuning $2\delta\omega$. The two eigen frequencies of Equation (19) are given by

$$\tilde{\omega}_{\pm} = \omega_c - i[(\gamma_{c1} + \gamma_{c2}) \mp \sqrt{(\gamma_{c1} - \gamma_{c2})^2 + (\gamma_l)^2}] \tag{20}$$

Different from the real gauge-flux detuning that can induce anti-PT phase transition, here the imaginary gauge-flux detuning will keep the system always in the anti-PT phase with decay rate bifurcation. The effect of imaginary gauge flux is to tune the decay-rate bifurcation amount of the two hybridized modes by controlling the intrinsic decay rate of γ_l, as shown by Equation (20). Interestingly, as γ_l reaches a critical value under a specific imaginary gauge flux biasing

$$|\gamma_l| = |\gamma_{l,\text{critial}}| = 2\sqrt{\gamma_{c1}\gamma_{c2}} \tag{21}$$

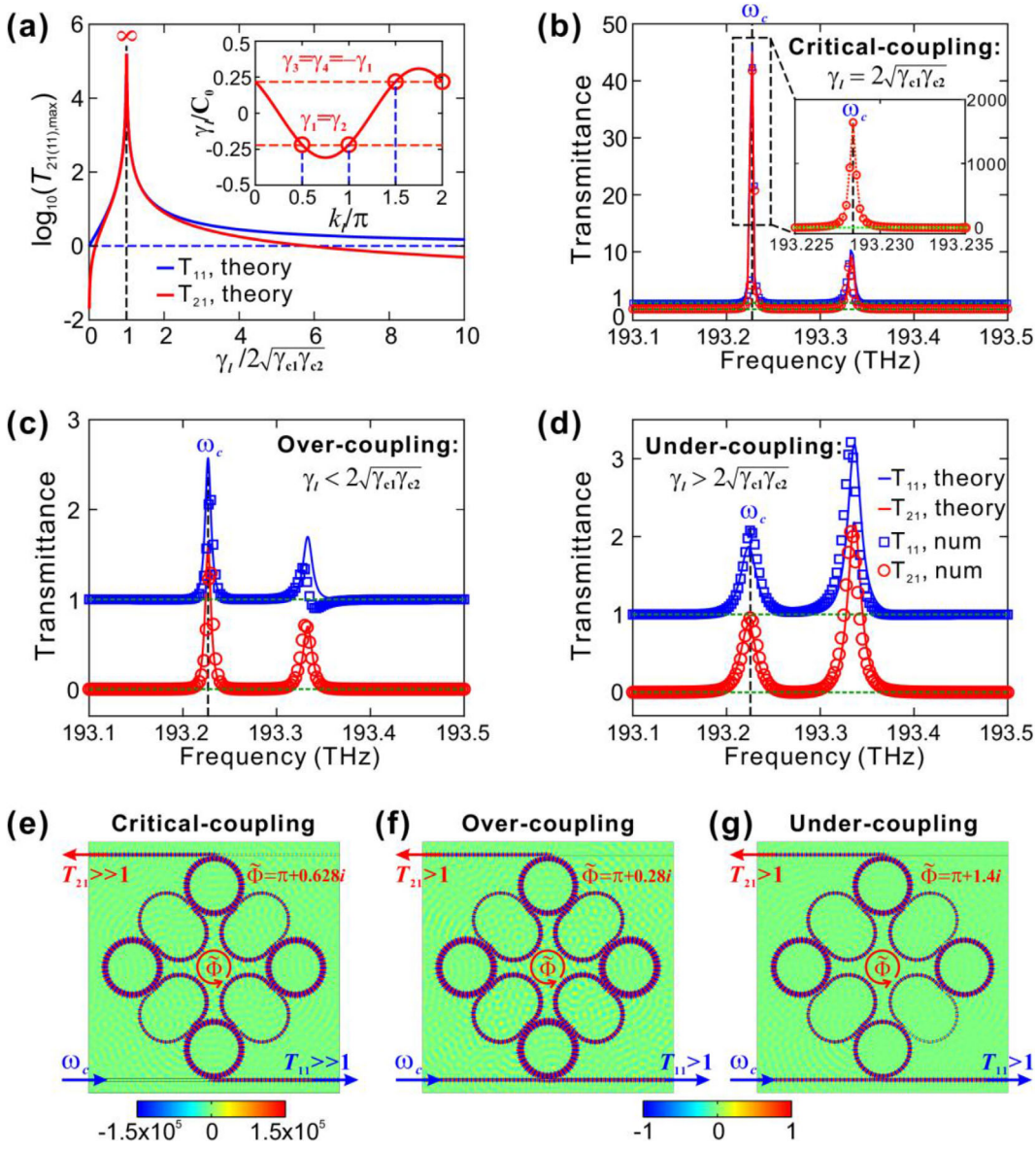

Figure 5. Channel-drop amplifying effects under an additional imaginary gauge-flux biasing. a) Logarithmic maximum transmittances T_{11} and T_{21} versus the imaginary gauge-flux induced intrinsic gain/loss rate γ_l. The inset figure shows the γ_l of the four Bloch modes, showing the opposite signs for the Bloch-mode pairs of $|\psi_2\rangle$, $|\psi_3\rangle$ and $|\psi_1\rangle$, $|\psi_4\rangle$. b,c,d) Channel-drop transmittance spectra under critical-coupling conditions and in the over-coupling and under-coupling regimes. In the three cases, the gaps are fixed at $g_1 = g_2 = 320$ nm, and the gauge flux is $\Phi = \pi + 0.628\,i$, $\pi + 0.28i$, and $\pi + 1.4i$ by choosing the imaginary refractive index $\delta n = 0.0022$, 0.001, and 0.005 in (b,c,d). e,f,g) Simulated field distributions for the excitation from the bottom waveguide at central frequency ω_c for the above three cases in (b,c,d).

the imaginary coupling rate between the two degenerate modes becomes $i(\gamma_{c1} + \gamma_{c2})$, which gives rise to two eigen frequencies

$$\tilde{\omega}_{\pm} = \omega_c - i(\gamma_{c1} + \gamma_{c2}) \pm i(\gamma_{c1} + \gamma_{c2}) = \begin{cases} \omega_c, \text{(lasing mode)} \\ \omega_c - i2(\gamma_{c1} + \gamma_{c2}), \text{(lossy mode)} \end{cases} \quad (22)$$

where the hybridized mode $|\psi_+\rangle$ exhibits a purely real eigen frequency ω_c, indicating that it has been pushed to the lasing threshold, dubbed as the **lasing mode**.[49,50] Meanwhile, the other hybridized mode $|\psi_-\rangle$ exhibits a larger decay rate of $2(\gamma_{c1} + \gamma_{c2})$ than the uncoupled decay rate of $\gamma_{c1} + \gamma_{c2}$ for each individual mode, indicating that it manifests as a **lossy mode**.

The excitation of the lasing mode can also be detected from the channel-drop tunneling transmittance spectrum (see Section S3 for detailed derivation, Supporting Information)

$$\begin{cases} T_{11}(\omega) = \dfrac{[4\gamma_{c1}\gamma_{c2} + (\omega-\omega_c)^2 + (\gamma_l)^2]^2 + [2(\omega-\omega_c)(\gamma_{c1}-\gamma_{c2})]^2}{[4\gamma_{c1}\gamma_{c2} - (\omega-\omega_c)^2 - (\gamma_l)^2]^2 + [2(\omega-\omega_c)(\gamma_{c1}+\gamma_{c2})]^2} \\ T_{21}(\omega) = \dfrac{16(\gamma_l)^2\gamma_{c1}\gamma_{c2}}{[4\gamma_{c1}\gamma_{c2} - (\omega-\omega_c)^2 - (\gamma_l)^2]^2 + [2(\omega-\omega_c)(\gamma_{c1}+\gamma_{c2})]^2} \end{cases} \quad (23)$$

which satisfies $T_{11}(\omega) > 1$, $T_{21}(\omega) > 1$ and $T_{11}(\omega) - T_{21}(\omega) = 1$, indicating the light amplification nature under the imaginary gauge-flux biasing and energy-difference preservation feature in the two waveguides. As $\gamma_l = \gamma_{l,\text{critical}}$, the transmission *pole* is reached at the real frequency ω_c, i.e., $T_{11}(\omega_c) = T_{21}(\omega_c) = \infty$, as shown in Figure 5a, verifying that the lasing threshold is reached. The occurrence of a transmission *pole* in the real frequency axis with infinite transmittance is a clear signature of the existence of the lasing mode. As γ_l deviates from $\gamma_{l,\text{critical}}$, either in the over-coupling regime, $\gamma_l < \gamma_{l,\text{critical}}$, or in the under-coupling regime, $\gamma_l > \gamma_{l,\text{critical}}$, the *pole* cannot reach the real frequency axis, which leads to a finite amplification in the channel-drop tunneling. Remarkably, the critical-amplifying behavior shares a similar physical nature with the critical-coupling concept for perfect light absorption in a single-port resonator, both of which require a match between the intrinsic and external decay rates.[51,52]

The simulated transmittance spectrum at the critical coupling point is shown in Figure 5b, which exhibits a very large amplification at the transmittance peak. Here the two gaps are still fixed at $g_1 = g_2 = 320$ nm, which gives rise to $\gamma_{c1} = \gamma_{c2} = 0.1C_0$. The complex refractive index is chosen as $n = n_0 \pm 0.0022i$ in the loss/gain parts of the auxiliary ring to get $\kappa = \text{Im}(n_{\text{eff}})k_0\pi R_2 = 0.157$ and hence $\Phi = \pi + iN\kappa = \pi + 0.628i$. Note that due to the presence of inevitable inaccuracies of the parameters, the simulated transmittance peak cannot reach infinite as the theory predicted. For comparisons, we also simulate the over-coupling and under-coupling cases by reducing or increasing the imaginary gauge flux to $\Phi = \pi + 0.28i$ and $\pi + 1.4i$ in Figure 5c,d by choosing $n = n_0 \pm 0.001i$ and $n = n_0 \pm 0.005i$ to get $\kappa = 0.07$ and 0.35, both of which manifest amplified channel-drop tunneling but with much lower amplifications. The simulated field distributions for the above three cases are shown in Figure 5e–g, where the lasing case exhibits a very large output-input ratio of $\approx 10^5$ while the other two cases show much lower ratios with comparable output-input magnitudes, thus verifying the above theoretical analysis for the lasing condition.

6. Conclusion

In summary, by applying gauge-flux biasing in a channel-drop, looped-resonator system, we achieve anti-PT phase transition and realize extreme control over channel-drop tunneling. As the real gauge-flux detuning varies, the system undergoes a phase transition between anti-PT and anti-PT-broken regimes, through which we achieve two extreme cases of complete channel-drop tunneling and complete tunneling suppression, realized by reaching the transmission zero or exciting the unidirectionally-decayed modes. Moreover, by introducing an imaginary gauge-flux biasing, we also achieve extreme channel-drop amplifying effects with giant amplification by reaching the transmittance pole of lasing mode under critical coupling conditions. Our work unveils a new strategy of applying a synthetic gauge field to induce anti-PT phase transition and realizes versatile extreme control over the channel-drop tunneling processes. The paradigm may stimulate further theoretical and experimental studies of applying photonic topological aspects to controlling non-Hermitian properties of light.

All these extreme channel-drop tunneling effects we develop may find potential applications in many different light-control scenarios. For instance, the ability to turn the transmittance spectrum from zero to unity can be used to develop tunable add-drop filters. The switching between complete channel-drop tunneling and complete tunneling suppression can be utilized to develop optical switches for light directional routing, wavelength demultiplexing, and signal processing. Moreover, the broadband complete tunneling suppression with all-pass features may be used to design optical buffers and delay lines for light storage and slow-light applications. In this case, since the light can be stored in the array with a long life time, it may also be used for optical sensing applications. Finally, the effect of giant light amplification during channel-drop tunneling can be harnessed to design active, non-Hermitian optoelectronic devices, such as gauge-flux-mediated microring lasers and high-ratio optical amplifiers.

In terms of experimental realizations, the passive, i.e., real gauge-flux-biasing microring resonator arrays can be realized based on the standard silicon-on-insulator (SOI) platforms with precise control of the geometries of auxiliary rings to provide the required gauge flux.[38,39,53] Meanwhile, the gap values between main and auxiliary rings as well as between main rings and bus waveguides should also be carefully designed to provide the required decay rates. Then, the imaginary gauge-flux-biasing resonator arrays can be realized based on active platforms with InGaAsP multiple quantum wells as the gain media and Cr/Ge layers on top of rings as the loss materials. We note that the integration of III–V material systems with silicon photonics platforms has been actively researched.[54,55] To provide the required gain/loss distribution, external light pumping with selectively pumped areas and pumped power should also be carefully controlled.[40,56,57]

Supporting Information

Supporting Information is available from the Wiley Online Library or from the author.

Acknowledgements

The work is supported by the National Natural Science Foundation of China (Grant No. 12204185, No. 12374305, No. 11974124, and No. 12021004), and the Natural Science Foundation of Hubei Province (No. 2022CFB036). S. F. acknowledges the support of MURI grants from the U. S. Air Force Office of Scientific Research (Grant No. FA9550-18-1-0379 and FA9550-22-1-0339).

Conflict of Interest

The authors declare no conflict of interest.

Data Availability Statement

The data that support the findings of this study are available from the corresponding author upon reasonable request.

Keywords

anti-PT symmetry, channel-drop tunneling, dissipative coupling, gauge field, microring resonator array

Received: May 22, 2023
Revised: September 12, 2023
Published online: January 22, 2024

[1] B. E. Little, S. T. Chu, H. A. Haus, J. Foresi, J.-P. Laine, *J. Lightw. Technol.* **1997**, *15*, 6.
[2] S. Fan, P. R. Villeneuve, J. D. Joannopoulos, H. A. Haus, *Phys. Rev. Lett.* **1998**, *80*, 960.
[3] S. Fan, P. R. Villeneuve, J. D. Joannopoulos, M. J. Khan, C. Manolatou, H. A. Haus, *Phys. Rev. B* **1999**, *59*, 15882.
[4] W. Jiang, R. T. Chen, *Phys. Rev. Lett.* **2003**, *91*, 213901.
[5] Z. Wang, S. Fan, *Phys. Rev. E* **2003**, *68*, 066616.
[6] W. Suh, S. Fan, *Appl. Phys. Lett.* **2004**, *84*, 4905.
[7] J. Wiersig, *Phys. Rev. Lett.* **2006**, *97*, 253901.
[8] K. Koshelev, S. Kruk, E. Melik-Gaykazyan, J. H. Choi, A. Bogdanov, H. G. Park, Y. Kivshar, *Science* **2020**, *367*, 288.
[9] L. Verslegers, Z. Yu, Z. Ruan, P. B. Catrysse, S. Fan, *Phys. Rev. Lett.* **2012**, *108*, 083902.
[10] C. W. Hsu, B. Zhen, J. Lee, S. Chua, S. G. Johnson, J. D. Joannopoulos, M. Soljačić, *Nature* **2013**, *499*, 188.
[11] C. W. Hsu, B. Zhen, A. D. Stone, J. D. Joannopoulos, M. Soljačić, *Nat. Rev. Mater.* **2016**, *1*, 16048.
[12] A. F. Sadreev, *Rep. Prog. Phys.* **2021**, *84*, 055901.
[13] H. Zhou, B. Zhen, C. W. Hsu, O. D. Miller, S. G. Johnson, J. D. Joannopoulos, M. Soljačić, *Optica* **2016**, *3*, 10.
[14] X. Yin, J. Jin, M. Soljačić, C. Peng, B. Zhen, *Nature* **2020**, *580*, 467.
[15] C. M. Bender, S. Boettcher, *Phys. Rev. Lett.* **1998**, *80*, 5243.
[16] K. G. Makris, R. El-Ganainy, D. N. Christodoulides, *Phys. Rev. Lett.* **2008**, *100*, 103904.
[17] C. E. Rüter, K. G. Makris, R. El-Ganainy, D. N. Christodoulides, M. Segev, D. Kip, *Nat. Phys.* **2010**, *6*, 192.
[18] S. K. Ozdemir, S. Rotter, F. Nori, L. Yang, *Nat. Mater.* **2019**, *18*, 783.
[19] L. Ge, H. E. Türeci, *Phys. Rev. A* **2013**, *88*, 053810.
[20] Y. Yang, Y.-P. Wang, J. W. Rao, Y. S. Gui, B. M. Yao, C.-M. Hu, *Phys. Rev. Lett.* **2020**, *125*, 147202.
[21] Z. Li, G. Cao, C. Li, S. Dong, Y. Deng, X. Liu, J. S. Ho, C. Qiu, *Prog. Electromagn. Res.* **2021**, *171*, 1.
[22] Q. Yan, H. Chen, Y. Yang, *Prog. Electromagn. Res.* **2021**, *172*, 33.
[23] P. Peng, W. Cao, C. Shen, W. Qu, J. Wen, L. Jiang, Y. Xiao, *Nat. Phys.* **2016**, *12*, 1139.
[24] Y. Jiang, Y. Mei, Y. Zuo, Y. Zhai, J. Li, J. Wen, S. Du, *Phys. Rev. Lett.* **2019**, *123*, 193604.
[25] Y. Choi, C. Hahn, J. W. Yoon, S. H. Song, *Nat. Commun.* **2018**, *9*, 2182.
[26] Y. Li, Y. Peng, L. Han, M. Miri, W. Li, M. Xiao, X. Zhu, J. Zhao, A. Alù, S. Fan, C. Qiu, *Science* **2019**, *364*, 170.
[27] F. Zhang, Y. Feng, X. Chen, L. Ge, W. Wan, *Phys. Rev. Lett.* **2020**, *124*, 053901.
[28] A. Bergman, R. Duggan, K. Sharma, M. Tur, A. Zadok, A. Alù, *Nat. Commun* **2021**, *12*, 486.
[29] X. L. Zhang, T. Jiang, C. T. Chan, *Light. Sci. Appl.* **2019**, *8*, 88.
[30] W. Liu, Y. Zhang, Z. Deng, J. Ye, K. Wang, B. Wang, D. Gao, P. Lu, *Laser Photonics Rev.* **2022**, *16*, 2100675.
[31] Z. Feng, X. Sun, *Phys. Rev. Lett.* **2022**, *129*, 273601.
[32] J. Zhang, Liu, Z. F., X. Sun, *Laser Photonics Rev.* **2023**, *17*, 2200079.
[33] H. Zhang, R. Huang, S. Zhang, Y. Li, C. Qiu, F. Nori, H. Jing, *Nano Lett.* **2020**, *20*, 7594.
[34] K. Fang, Z. Yu, S. Fan, *Phys. Rev. Lett.* **2012**, *108*, 153901.
[35] K. Fang, Z. Yu, S. Fan, *Nat. Photon.* **2012**, *6*, 782.
[36] Q. Lin, S. Fan, *Phys. Rev. X* **2014**, *4*, 031031.
[37] C. Qin, F. Zhou, Y. Peng, D. Sounas, X. Zhu, B. Wang, J. Dong, X. Zhang, A. Alù, P. Lu, *Phys. Rev. Lett.* **2018**, *120*, 133901.
[38] M. Hafezi, E. A. Demler, M. D. Lukin, J. M. Taylor, *Nat. Phys.* **2011**, *7*, 907.
[39] M. Hafezi, S. Mittal, J. Fan, A. Migdall, J. M. Taylor, *Nat. Photon.* **2013**, *7*, 1001.
[40] H. Zhao, X. Qiao, T. Wu, B. Midya, S. Longhi, L. Feng, *Science* **2019**, *365*, 1163.
[41] C. Qin, A. Alù, Z. J. Wong, *ACS Photonics* **2022**, *9*, 586.
[42] S. Longhi, D. Gatti, G. D. Valle, *Phys. Rev. B* **2015**, *92*, 094204.
[43] S. Longhi, *Phys. Rev. A* **2016**, *94*, 022102.
[44] S. Fan, W. Suh, J. D. Joannopoulos, *J. Opt. Soc. A* **2003**, *20*, 569.
[45] W. Suh, Z. Wang, S. Fan, *IEEE J. Quant. Elec.* **2004**, *40*, 1511.
[46] F. Alpeggiani, N. Parappurath, E. Verhagen, L. Kuipers, *Phys. Rev. X* **2017**, *7*, 021035.
[47] A. Krasnok, D. Baranov, H. Li, M. Miri, F. Monticone, A. Alù, *Adv. Opt. Photon.* **2019**, *11*, 892.
[48] C. Sauvan, J. P. Hugonin, I. S. Maksymov, P. Lalanne, *Phys. Rev. Lett.* **2013**, *110*, 237401.
[49] H. Schomerus, *Phys. Rev. Lett.* **2010**, *104*, 233601.
[50] Y. D. Chong, L. Ge, A. D. Stone, *Phys. Rev. Lett.* **2011**, *106*, 093902.
[51] M. Cai, O. Painter, K. J. Vahala, *Phys. Rev. Lett.* **2000**, *85*, 74.
[52] A. Yariv, *IEEE Photonics Technol. Lett.* **2002**, *14*, 483.
[53] S. Mittal, E. A. Goldschmidt, M. Hafezi, *Nature* **2018**, *561*, 502.
[54] L. Chang, S. Liu, J. Bowers, *Nat. Photon.* **2022**, *16*, 95.
[55] C. Xiang, W. Jin, O. Terra, B. Dong, H. Wang, L. Wu, J. Guo, T. Morin, E. Hughes, J. Peters, Q. Ji, A. Feshali, M. Paniccia, K. Vahala, J. Bowers, *Nature* **2023**, *620*, 78.
[56] M. A. Bandres, S. Wittek, G. Harari, M. Parto, J. Ren, M. Segev, D. N. Christodoulides, M. Khajavihkhan, *Science* **2018**, *359*, 4005.
[57] Z. Wong, Y. Xu, J. Kim, K. O'Brien, Y. Wang, L. Feng, X. Zhang, *Nat. Photon.* **2016**, *10*, 796.